Modelling and evaluation of the micro abrasive blasting process

M. Achtsnick [a,*], P.F. Geelhoed [b], A.M. Hoogstrate [a], B. Karpuschewski [a]

[a] *Laboratory for Production Technology and Organisation, Delft University of Technology, Mekelweg 2, 2628 CD Delft, The Netherlands*
[b] *Laboratory for Aero and Hydrodynamics, Delft University of Technology, Mekelweg 2, 2628 CD Delft, The Netherlands*

Abstract

Micro abrasive blasting (MAB) is becoming an important machining technique for the cost effective fabrication of micro devices. The material removal process is based on the erosion of a mask-protected brittle substrate by an abrasive-laden air jet. To exploit the potentials of this technique for applications of industrial interest, the blasting process has to become more efficient and better predictable. Therefore, in this paper micro-abrasive blasting is analysed by means of a set of models containing different sub-models for the particle jet, the erosion mechanisms of a single particle impact and the machining results.

A one-dimensional isentropic flow model was developed to calculate the particle exit velocity of each individual particle in the airflow for two different types of nozzles: a converging cylindrical and a new developed line shaped Laval-type. The particle size and its position within the air jet are based on probability distribution functions. The result is a nozzles characteristic energy intensity distribution of the particle beam. Subsequently, classical indentation fracture mechanics is used to model the interaction between incoming particles and the substrate surface. The simulation shows that the Laval-type nozzle is able to increase the particle velocity with more than 30% compared to the converging nozzle. Also the blasting profile is more uniform with a relatively flat bottom.

Experimental verifications of the particle velocities using particle image velocimetry (PIV) and measurements of the roughness and the shape of the blasting profile demonstrate that the presented model is capable to predict accurately the blasting performance of both nozzles types.

1. Introduction

Micro abrasive blasting (MAB) is a promising technique to structure and perforate brittle and hard materials. A main field of application is the realisation of economically viable micro electro mechanical systems (MEMS) [1–3]. MAB introduces the concept of precision machining techniques to conventional blasting through the use of fine and hard abrasives, constant powder feeding devices and masking technology. In contrast to direct blasting, the surface is exposed completely to the erosive action of the particle beam. Hence, before processing, the substrate material has to be partially shielded by applying an erosion resistant mask. Only where

the mask does not protect the workpiece, material removal will take place. During processing an air pressure between 0.2 and 0.9 MPa and angular ceramic particles with diameters between 10 and 100 μm are employed.

The mask determines the accuracy of the surface structure in the plane dimensions [4]. To control the depth of the structure, the surface has to be uniformly covered with abrasives. Therefore, a constant powder flow and the scan strategy of the nozzle with respect to the workpiece surface are of great importance. The particle dispersion and the velocity profile of the beam determine the shape of the blasting profile.

The fluid flow conditions in the blasting nozzle have been identified early as one of the most vital elements to control erosion [5]. Numerous empirical studies on particle velocity arrived later on investigating the influence of nozzle length [6], and roughness [7], particle loading ratio, distance from

* Corresponding author. Tel.: +31 15 2781318; fax: +31 15 2783910.
 E-mail address: m.achtsnick@wbmt.tudelft.nl (M. Achtsnick).

the nozzle exit and radial position of the particles [8,9]. Equations have been derived to show that the blasting profile using cylindrical nozzles is reverse bell mouthed in shape [10,11].

Recently, the abrasive blasting process has been analytically modelled in terms of erosion efficiency and blasting profile [12,13]. Based on these results a simple Monte Carlo simulation has been developed to predict roughness and erosion rate [14]. However, most of these models relate input parameters directly to output characteristics by one complex model. This complicates the possibility to verify modelling steps, to integrate different modelling methods and to adapt the model to different input situations.

The objective of the following paper is to extend the computational set of models as developed in [15]. At first, an improved Laval-type blasting nozzle is presented. Subsequently, the construction of a set of models for MAB is outlined. As input model, probability based distribution functions of the particles are combined with a fluid flow model. Two different nozzle configurations are implemented to the input model. The following process model makes use of classical fracture mechanics to describe the material removal process. The underlying fracture mechanism is based on the crack pattern evoked by a single angular particle that indents a flat surface. The final output model demonstrates that the shape and the roughness of the microstructure can be influenced with the nozzle configuration. Verification measurements for both, input and output model complete this work.

2. Blasting nozzles

Available blasting equipment often uses nozzles with cylindrical cross-section and converging blast duct that limits the airflow velocity to the speed of sound. Due to the presence of a boundary layer, the particle velocity and the amount of particles are higher near the centreline of the beam than those close to the nozzle wall [16]. As a consequence, the machining result is difficult to control. For bigger round nozzles a decrease in efficiency has been noticed due to the flux effect [17]. Furthermore, available pressure feeding systems show lacks through an unsteady particle flow rate.

To overcome these shortcomings of converging and round nozzles, the following demands on an improved nozzle design have to be fulfilled:

- pressure-less constant feeding system;
- supersonic airflow velocity in the nozzle;
- homogeneous dispersion of abrasive particles over the width of the nozzle; and
- long lifetime of the nozzle.

In order to meet these requirements, a Laval-type nozzle with a line-shaped orifice has been designed [18]. It is expected that a line-shaped orifice minimizes the flux effect and delivers better machining results due to a homogeneous distribution of the particle flow perpendicular to the machining direction. The internal Laval geometry is able to increase the airflow velocity beyond 1 Mach. Furthermore, a Laval-type nozzle allows creating vacuum pressure in the duct that enable a suction feeding system for abrasives.

The new blasting nozzle is realised as a "sandwich" with bottom and top plate and an interchangeable internal plate representing the Laval geometry. The internal geometry is depicted together with the complete nozzle design in Fig. 1. The thickness of the internal plate was 3 mm but can be adapted to the available compressor capacity.

To avoid disturbances of the flow the particle inlet is arranged in the centre of the backside between two air inlets. The nozzle duct is coated with a ceramic layer to increase lifetime. The internal geometry was designed for over-expanded flow with a cross-section area relation A_{exit}/A_{throat} of 10.3 delivering an airflow velocity of $Ma = 3.34$. With these design specifications the nozzle should achieve supersonic flow beyond inlet pressures of 0.55 MPa without shock wave in the duct. In order to give the abrasive particles ample time to accelerate the diverging part was made rather long (75 mm).

3. Model construction

To describe the overall process, the following set of models makes use of a modular approach with different sub models, which are built around a central process model (Fig. 2).

The advantage of such a construction is a simple evaluation and verification of subsequent modelling steps and a possible integration of different modelling methods e.g. an analytical description of the material removal mechanism with a
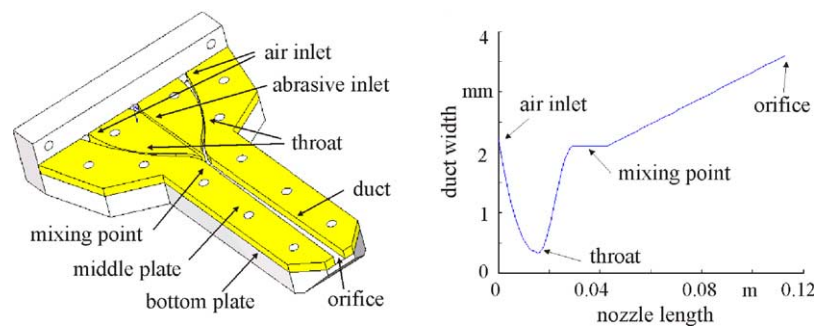

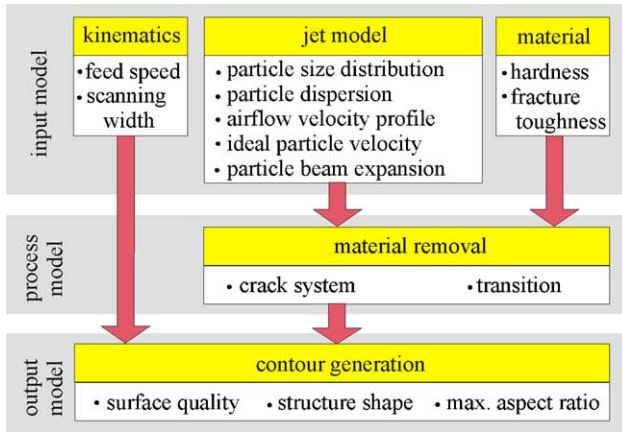Fig. 1. Laval nozzle design. The top plate is removed.

Fig. 2. Set of models for MAB.

Fig. 3. Particle size distribution for alumina mesh 360.

stochastic distribution based jet model. All of the sub-models are adaptable to a specific machining situation.

In MAB the local impact conditions vary for each particle impact. Therefore, the input model has the objective to provide the energy and the position of each individual particle in the jet. It is composed of the particle size and dispersion model, the modelled airflow velocity profile, the particle velocity calculation and the beam expansion model. The kinematic model provides information about the relative motion between the substrate surface and the particle beam. As a result, the input model has to yield to a characteristic energy intensity distribution giving a fingerprint of a nozzle for each input situation.

The process model describes, with the aid of the material model, the interaction between impinging particles and the substrate surface. Due to the nature of the blasting process and to simplify the simulation routine, each impact is considered to be perpendicular. Indentation fracture mechanics is used to analyse the formation of subsurface lateral cracks in order to estimate the material loss. Therefore, the kinetic energy of a single particle is equated with the plastic work done during impact. The transition from plastic deformation to brittle fracture is controlled by properties of the substrate material. The output model reflects the shape of the blasting profile and the quality of the machined surface.

4. Jet model

MAB technology makes use of alumina as blasting material since it combines a high hardness and good cutting ability with a rather low price.

In Fig. 3 the measured equivalent spherical diameter of white fused alumina mesh 360 is indicated (Malvern, Mastersizer 2000). The second curve represents a truncated normal distribution fitted to the distribution points of ISO 8486; d_{par} (0.5), d_{par} (0.94), and d_{par} (0.03). The fitted function yields a mean of 21.6 μm with a standard deviation of 4.6 μm.
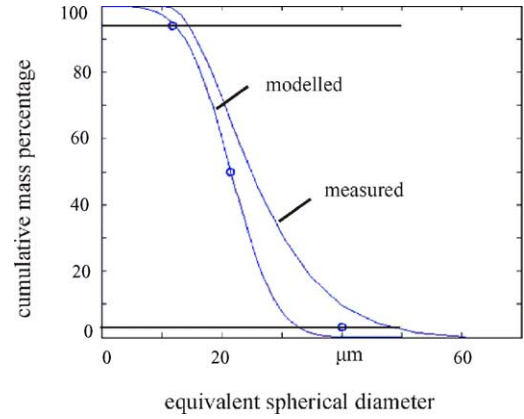
For both nozzles, the particle dispersion within the beam has been fitted to experiments counting the number of particle impacts per area. These experiments and previous work [9] have confirmed that the particle dispersion depends on the nozzle type. Cylindrical nozzles generate an axis symmetrical normal distribution. Whereas, the Laval nozzle spreads the particles more homogeneously over the width due to its line shaped orifice and its internal geometry. The distribution function of the Laval nozzle is gained by superimposing a normal and a uniform probability density function. Each particle in Fig. 4 is drawn regardless its true size.

The area of the blast spot A_S is given by the nozzle dimensions (x_0, y_0), the dispersion angle δ and the nozzle tip distance (NTD) by

$$A_S = 2 \tan(\delta) \text{NTD}(x_0 + y_0) \tag{1}$$

Observing the dispersion angle one can distinguish between the core and total jet angle. In this investigation the core jet angle has been defined by the impact area with an erosion depth of more than 10% of the total blasting depth. Experiments measuring the impact area of a stand still nozzle with a known NTD have shown that the core jet expands with 3.5° for both nozzles. The total jet expands with about 7° schematically drawn in Fig. 5. Since the nozzle dimensions of the Laval nozzle are nearly twice of the cylindrical nozzle, its NTD has bee doubled as well. For simplifying reasons in the model, the particle trajectories in the stream are considered to follow a straight line and no particle rotation has been supposed.

Airflow conditions of both a fully supersonic and a subsonic nozzle can be calculated using the standard equations for one-dimensional compressible isentropic flow through a duct with the standard properties of gas listed in Table 1 [19].

Subsequently a program has been written to calculate each particle exit velocity in a one-dimensional compressible flow through a duct [20]. It is assumed that the drag force $F_{D,i}$ is the main force of acceleration calculated by

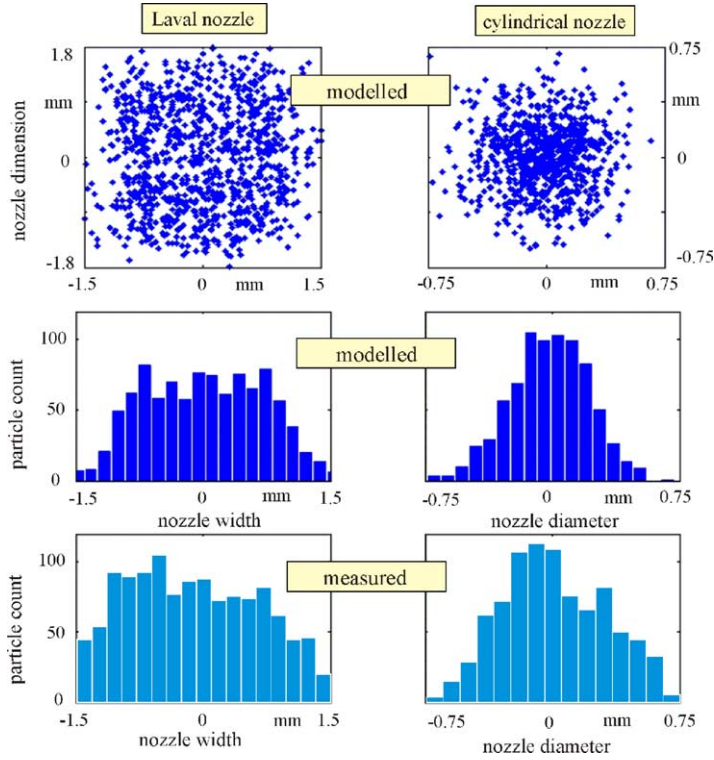$$F_{D,i} = \frac{1}{2} C_{D,i} \rho_i v_{rel,P,i}^2 A_P \tag{2}$$

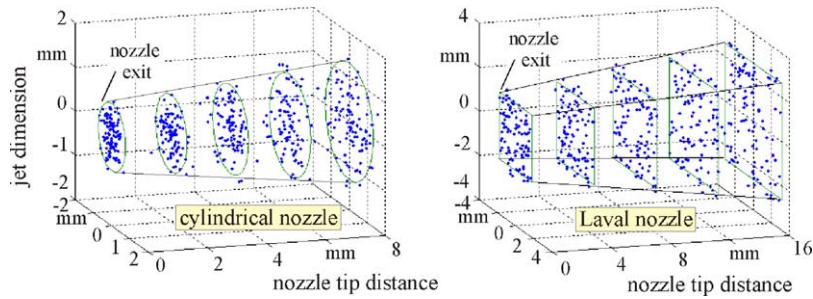Fig. 4. Modelled and measured particle density distribution at the exit of both nozzles.

Fig. 5. Modelled particle dispersion and jet expansion after leaving the nozzle.

with the local drag coefficient of a sphere $C_{D,i}$, local air density ρ_i and the particle surface area A_P. The local relative particle velocity $v_{rel,P,i}$ is related to the local airflow velocity.

The model uses the common simplifications: particle–particle and particle–wall interactions are excluded and the shape of the particles is considered to be spherical. The loading ratio, defined as the quotient of particle and air flux, was

Table 1
Properties of gas

Ambient exit pressure (Pa)	1×10^5
Specific heat ratio of air	1.4
Dynamic viscosity of air at T_0 (kg/m s)	2.07×10^{-5}
Sonic speed at entrance (m/s)	343
Gas constant (J/kg K)	286.86
Gas stagnation temperature, T_0 (K)	293
Atmospheric density (kg/m^3)	1.225

sufficiently small (0.1) to ignore the momentum transfer from the gas to the particles [20].

Often flow models neglect that the drag coefficient depends on both, Reynolds number Re and on local relative Mach number $Ma_{rel,i}$. In this model an interpolation-routine estimates the local $C_{D,i}$ values and includes the results as look-up table in the simulation. The experimental data set for the look-up table was digitised from [21] and plotted in Fig. 6. It can be noticed that an enhancement of the relative Mach numbers beyond 1.5 has little beneficial influence on the drag coefficient for Reynolds numbers beyond 10^4.

Knowing the local particle drag force, the velocity of each individual particle can be calculated step-by-step downstream through the nozzle by

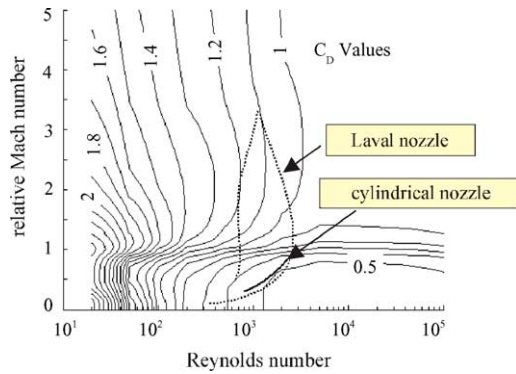$$v_j = \sqrt{v_i^2 + 2v_i' \, \mathrm{d}s} \tag{3}$$

Fig. 6. Used sphere drag coefficient dependent on *Re* and *Ma* [24].

Fig. 7 demonstrates the calculated airflow conditions and the resulting velocity of a mean particle along the nozzle length of the Laval nozzle.

The maximal airflow velocity occurs only at the centre line of the beam and stays constant within the core jet region [19]. To consider the influence of a boundary layer between air and nozzle wall the maximal air velocity v_{max} away from the centre line (x, y) is reduced accordingly to the turbulent airflow velocity profile through a duct. The velocity profile of round and square nozzles with Reynolds numbers $Re < 10^5$ is paraboloidal in shape and follows the power law of Prandtl

$$v_{turbulent}(x, y) = v_{max}(x, y)^n \tag{4}$$

with the exponent $n = 1/7$ [22]. The particle trajectories follow the jet expansion angle. At the point of impact the dis-

tance of each particle from the centre line is calculated and its velocity reduced accordingly to $v_{turbulent}(x, y)$. In a converging nozzle particles continue to accelerate downstream [1].

The spots in Fig. 8 represent the calculated velocities of 25 random generated particles gained from the size and position distribution for different inlet pressures. For the cylindrical nozzle the total length of acceleration is composed of the nozzle length itself and of the NTD. The acceleration length of the Laval nozzle is determined through the distance of particle mixing point and nozzle exit. In the case of the cylindrical nozzle an increase of the inlet pressures yields slightly higher particle velocities. Accordingly, with the air density the drag force on the particle increases. However, due to its converging duct the air velocity is limited to the speed of sound resulting in maximum particle velocities of 222 m/s with an average of 201 m/s for 0.8 MPa inlet pressure. In opposite, the Laval nozzle achieves supersonic airflow conditions from 0.6 MPa, visible in the significant increase of the particle velocity between 0.5 and 0.6 MPa. The maximum particle velocity is calculated with 376 m/s leading to an average of 292 m/s for 0.8 MPa inlet pressure.

To verify the simulation results, particle image velocimetry (PIV) has been employed because it delivers instantaneous full-field velocity information [23]. A pulsed laser light sheet is used to illuminate the particles in the flow. The light, scattered by the particles, has been recorded by a camera for image detection with a delay of 1 μs. By analyzing the travel length Δx of a certain particle located on x at time t, over a short time interval Δt, the local velocity of a particle v_P can
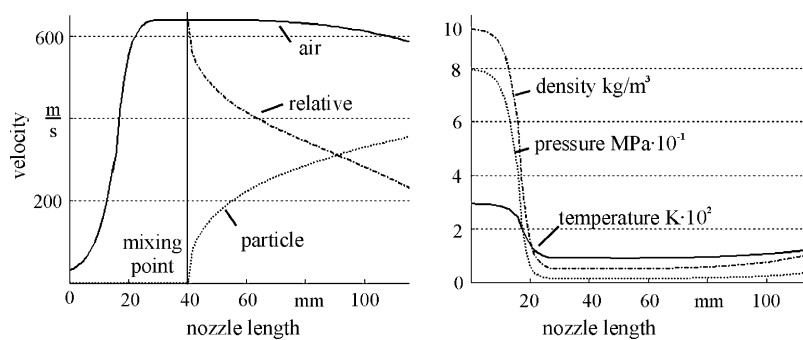

Fig. 7. Modelled flow properties along the nozzle duct of the Laval nozzle.
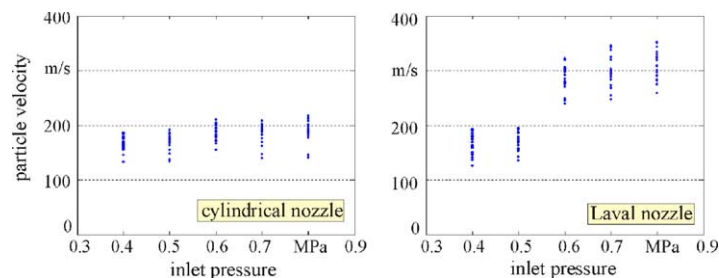

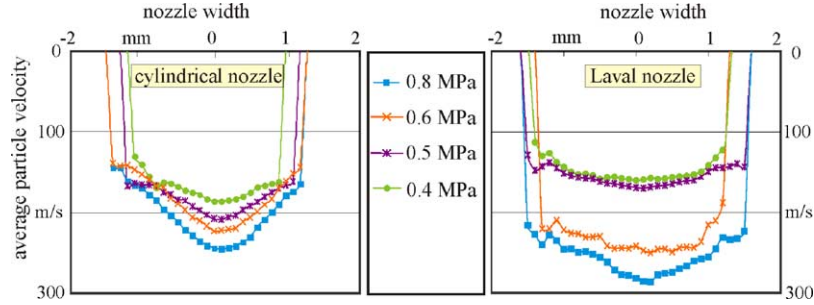Fig. 8. Modelled particle velocities over a range of different inlet pressures.

Fig. 9. Measured axial velocity profiles of both nozzles.

be calculated by

$$v_P(x, t) = \frac{\Delta x(x, t)}{\Delta t}$$ (5)

An interrogation window size of 64×64 pixels, representing the measurement values, were filtered and averaged by means of a PIV algorithm for estimating time-averaged velocity fields [24]. Ensemble correlation has been used to increase the reliability of the particle velocity estimation. The camera/lens combination had a measurement volume of $11\,\text{mm} \times 8.3\,\text{mm} \times 0.5\,\text{mm}$ corresponding to 42 vectors in width and 32 in height. Laser beam and camera were focused at the middle of the beam 12 mm downstream from the nozzle exit. The used abrasives were the same as in the simulation, alumina mesh 360.

Fig. 9 shows the results of the PIV measurements for a range of inlet pressures. It is visible that the Laval nozzle achieves a maximum average particle velocity of 290 m/s. According to the predictions, the airflow becomes supersonic from 0.6 MPa. The particle velocity at 0.8 MPa exhibits a deviation of only 20% along the width of the nozzle exit. For the same pressure, the cylindrical nozzle shows a maximum particle velocity of 240 m/s and a deviation of about 60% over the nozzle width, resulting in the typical bell mouthed shape. In terms of particle velocity the predictions for both nozzles fit very well with the measurement results.

In a last modelling step velocity, mass, and position of an individual particle within the beam are combined to an energy intensity distribution. The simulation assumes a NTD of 8 mm for the cylindrical, 16 mm for the Laval nozzle and an inlet pressure of 0.8 MPa for both nozzles.

Each dot in the resulting plot in Fig. 10 represents a discrete particle having an amount of energy at a certain position. The particle beam for the cylindrical nozzle is characterized by a high number of particles with higher energy values in the core of the jet. Fewer particles having lower energy values are to distinguish in the outer regions of the beam. The particle beam of the Laval nozzle shows an evenly spread and more homogeneously dispersed profile with in total higher energies per particle.

5. Model of the material removal

Marshall et al. developed a fracture system involving elastic–plastic behaviour of the substrate material [25]. It is generally agreed that beneath a loaded indenter, a plastically deformed zone is developed. The tip of the indenter has to be perfectly sharp to achieve a stress singularity at this point. For simplicity hardness is interpreted in the model as invariant for substrate and particle material. The condition that the particle hardness has to be higher than the substrate hardness is fulfilled for the presented situation.

Generally the Vickers hardness HV is defined as the ratio of indenter force P and surface of the indention A. The surface replaced by its Vickers representation and the load, expressed dependent on the indention depth h leads to
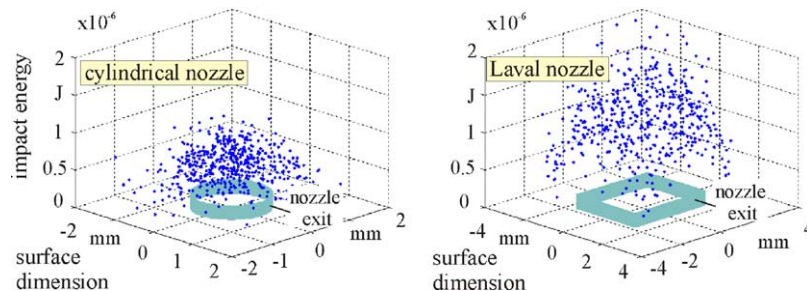
$$P(h) = \frac{2\text{HV}\,a^2(h)}{\sin \alpha}$$ (6)

Fig. 10. Energy intensity distribution of 500 particles for 0.8 MPa.

a is the half of the indention diagonal length and 2α the plane angle of the indenter. The plastic work W_{substr} done during impact can be equated with

$$W_{plastic,substr} = \int_0^{h_{max}} P(h)\,dh$$
$$= \int_0^{h_{max}} HV\,A(h)\,dh = HV\,\delta V \qquad (7)$$

with the indentation volume of a pyramid

$$\delta V = \frac{1}{3}Ah \qquad (8)$$

Assuming complete inelastic collision with $U_{kin,P} = U_{plastic,substr}$ and expressing h in terms of a gives

$$U_{kin,P} = \frac{2}{3}\frac{a^3 HV}{\sqrt{2}\tan\alpha} \qquad (9)$$

Inserting (6) in (9) results in the peak load during impact

$$P_{max} = \sqrt[3]{\frac{36HV\,U_{kin,P}^2\,\tan^2\alpha}{\sin\alpha}} \qquad (10)$$

The indention length a and the radius of the plastically deformed zone b can be correlated via the Hill model of the expanding cavity in a perfect plastic material with [26]

$$\frac{b}{a} = \mu\left(\frac{E}{HV}\right)^m \qquad (11)$$

where m is a dimensionless constant, traditionally $m = 1/2$. More recent investigations suggest $m = 0.43$ in a similar situation to be more appropriate [12], so it is used here.

If the applied load exceeds the threshold value P_0 the dislocation density reaches its critical limit and a radial crack will propagate downwards from the base of the plastic zone. On unloading, the radial crack closes and driven by residual stresses lateral cracks arise.

Once initiated, the lateral crack propagates on a plane parallel to the substrate surface. In homogeneous and isotropic materials, the cracks eventually grow upwards detaching finally a chip.

The propagation of the cracks is controlled by tensile stresses. Evans et al. [27] have shown that the tensile stresses that cause lateral fracture are at a maximum near the elastic–plastic boundary. Thus, it has been concluded that the depth at which lateral cracks initiate is equal to the depth of the plastic zone b (Fig. 11).

The equilibrium crack size c_L can be expressed as a function of the applied load with [25]

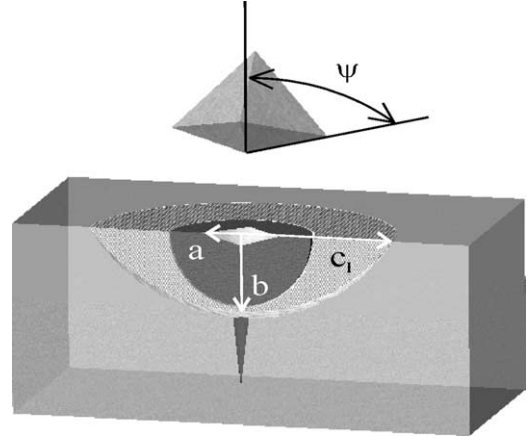$$c_L = c^L\left[1 - \left(\frac{P_{0a}}{P}\right)^{1/4}\right]^{1/2} \qquad (12)$$

Fig. 11. Crack system after [25].

where c^L represents a crack function related to the top angle between the pyramidal edges ψ

$$c^L = \left[\left(\frac{\zeta_L}{A^{1/2}}\right)(\cot\psi)^{5/6}\left\{\frac{(E/HV)^{3/4}}{K_C\,HV^{1/4}}\right\}\right]^{1/2} P^{5/8} \qquad (13)$$

and P_{0a} the apparent threshold

$$P_{0a} = \alpha_2\left(\frac{K_C}{HV}\right)^3 K_C\left(\frac{E}{HV}\right) \qquad (14)$$

with

$$\alpha_2 = \left(\frac{\zeta_0}{A^2}\right)(\cot\psi)^{-2/3} \qquad (15)$$

E is the elastic modulus and K_C the fracture toughness of the substrate. The compliance coefficient A in Eq. (13) indicates that lateral crack extension should not be strongly influenced by preformed radial cracks and is given with 0.75 for long, well developed cracks. ζ_L und ζ_0 are adjustable, dimensionless constants, independent of the material/indenter system. Marshall calibrated them to $\zeta_L = 25 \times 10^{-3}$ and $\zeta_0 = 1.2 \times 10^3$ [25]. Beyond the load P_{0a} the lateral crack becomes visible outside the plastic zone. For that reason the equations are only valid for larger cracks.

Using borosilicate glass with the material properties summarised in Table 2 results in modelled lateral crack lengths plotted in Fig. 12. In extension to [25] the graph gives crack lengths for very low particle loads as obtained with MAB.

This modelling approach has been verified exemplarily on a single crack level for alumina particles mesh 360. Fig. 13 shows crack patterns after processing glass with 0.8 MPa using a light microscope on the left-hand side and white light

Table 2
Material properties of borosilicate glass AF45

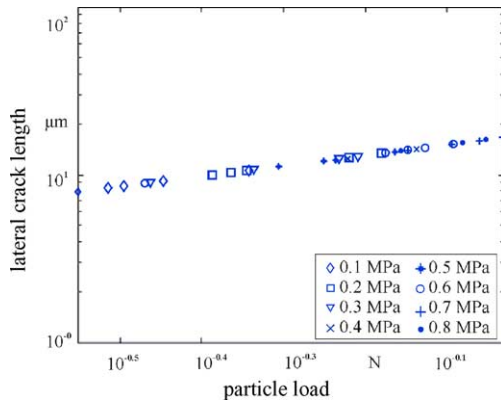|	
Elastic modulus E (Pa)	6.61×10^{10}
Vickers hardness HV (Pa)	5.13×10^9
Fracture toughness I mode K_{ic} (Pa m$^{1/2}$)	8.5×10^5
Specific weight ρ (kg/dm^3)	2.727

Fig. 12. Modelled lateral crack dimension.

interferometer on the right. Even though the impressions are arbitrarily the crack dimension seems well representative but rather seldom to find in this completeness.

6. Material erosion

If the particle impact exceeds the threshold for crack initiation and non-interacting crack patterns are assumed, the volume of the chip removed from the substrate by a single particle V_{cap} can be taken as spherical cap calculated with

$$V_{cap} \frac{1}{6} \pi b (3 c_{L}{}^{2} + b^2) \qquad (16)$$

This leads to the dimensionless erosion rate E_{rat} expressed by the removed mass of the substrate related to the mass of the particles.

$$E_{rat} = \frac{V_{cap} \cdot \rho_p}{m_p} \qquad (17)$$

Fig. 14 presents the modelled erosion rate of single particles dependent on their velocity and impact energy. Different inlet pressures of the cylindrical nozzle are used in the model to vary impact energy. The fitting lines have been obtained using a power law fit giving a velocity exponent of 2.2 and a kinetic energy relation of $4U_{kin}^{0.64}$. It becomes visible that the erosion rate is not a function of the particle energy only [12]. Following the model, more impact energy is needed for bigger particle diameters to achieve the same erosion rate. The threshold for lateral cracking of glass being 1.7 nJ [28] is not of influence for the modelled input parameters.

Verification measurements under the same conditions as in the simulation have demonstrated that the sum of all single impact events plotted in Fig. 14 overestimates the total erosion rate about 70 times. Obviously, smaller effective impact angles at the flank of the blasting profile and losses due to the probability of fracture, interferences between rebounding and incoming particles and intersections between the chips reduce the erosion efficiency significantly. However, a relation like Eq. (17) gives a good indication of the removal process and can be considered as ideal situation. Furthermore, the modelled chip depth can be used to predict the blasting profile and the achievable surface roughness.
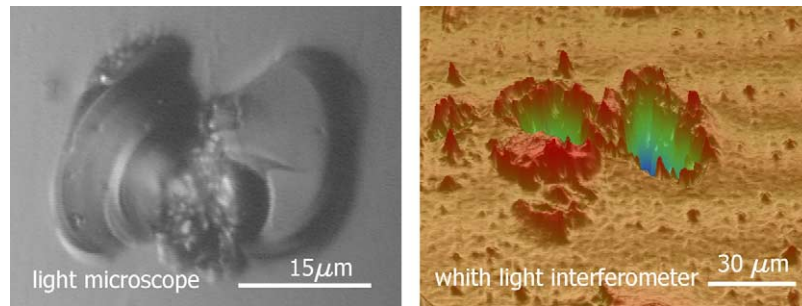

Fig. 13. Crack lengths dimensions in glass after processing with 0.8 MPa.
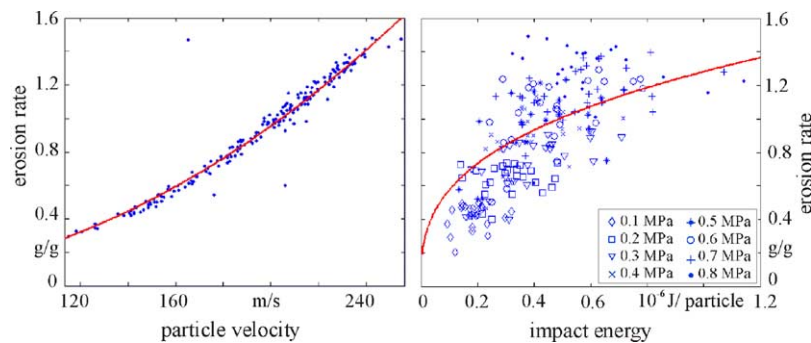

Fig. 14. Modelled erosion rate of particles plotted against its velocity and impact energy.
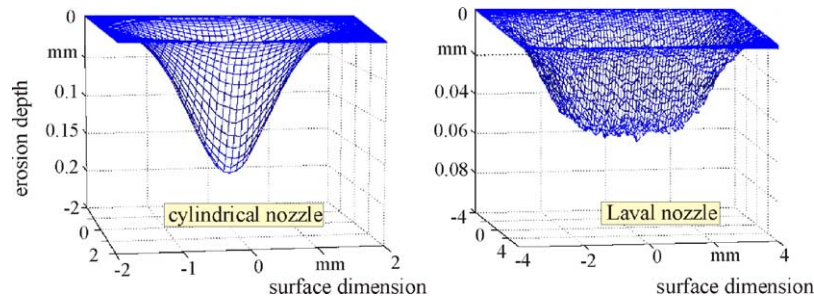
Fig. 15. Blasting profiles with a stand still nozzle.

7. Blasting profile

As the output model, the energy intensity distribution of previously defined particles is used to determine the profile of the blasted microstructure. Therefore, the substrate surface has been modelled with a grid having a resolution of 60×60 nodes on an area of $2\,\text{mm} \times 2\,\text{mm}$ for the cylindrical nozzle and 120×120 nodes on an area of $4\,\text{mm} \times 4\,\text{mm}$ for the Laval nozzle. For the generation of shapes only the depth of a removed chip and the number of impacts is of importance.

In Fig. 15 the simulation is processed in glass with two million particles each. The modelling conditions were the same as used for the energy intensity distribution. Both plots show the characteristic wall inclination angle for blasting profiles. Since fewer particles per area are hitting the surface the Laval nozzle displays a lower total erosion depth. However, its blasting profile is more evenly spread with a rather plain area in the middle of the bottom. Using this area for the development of a scan strategy during blasting it becomes possible to remove material more evenly and controlled.

In order to verify the resulting blasting profile, machining tests with both nozzles have been carried out. Fig. 16 shows cross-sectional profiles of single nozzle scans in glass with an inlet pressure of 0.8 MPa and a NTD of 12 mm. The feed speed for both settings was 0.5 mm/s with a powder flow rate of 20 g/min for the Laval and 5 g/min for the cylindrical nozzle. With these settings the particle impact density is uncritical and interference effects of incoming and rebounding particles can be neglected [29]. The topography has been measured employing a stylus tip device.

The blasting tests have proven that the predictions of the model with respect to the blasting shape fits very well. No-

tably, due to its line shaped blasting profile the Laval nozzle exhibits a large area in the center where the variations in depth are smaller than 10 μm allowing predictable and uniform material removal.

8. Roughness modelling

Since most of the applications using MAB are sensitive to surface quality, it is of great relevance to model the achievable surface roughness. The objective is to control the surface roughness by means of process parameters e.g. inlet pressure. In this work comparisons of the roughness of a blasted surface were made for different inlet pressures for both modeled and measured values. The modeled values have been obtained using a simulated blasted surface. An algorithm has been applied to hinder particle continually impacting on the same point. Achieving a set of numerical data, the trapezoidal rule can be used to calculate the roughness average Ra.

$$\text{Ra} = \frac{1}{N} \sum_{n=1}^{N} |Z_n| \qquad (18)$$

Experimental data were obtained respectively with a stylus tip profile meter (Talysurf, Taylor Hobson) and a white light interferometer (Wyko HD 8000, Veeco). All experimental and modeled values were filtered using a Gaussian high pass filter with a cut off length of 0.8 mm.

The left-hand side of Fig. 17 demonstrates the modeled surface with Ra indicated. In the data plot on the right hand, it is visible that surface roughness increases linearly with particle velocity. Since the prediction is based on the maximum
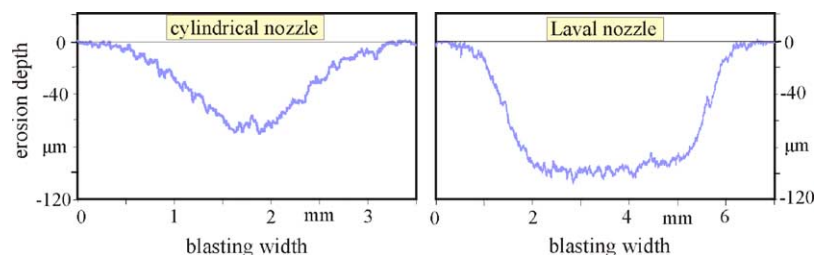

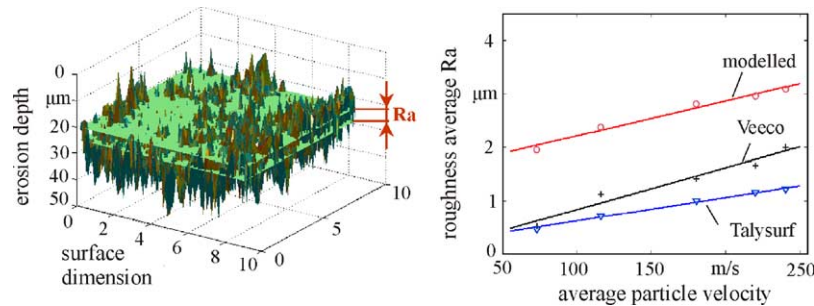Fig. 16. Measured cross-section of both blasting profiles.

Fig. 17. Surface roughness average modeled and measured for different particle velocities.

chip depth, the model overestimates the measured roughness slightly. During experimental verification, the stylus tip device tends to measure for higher particle velocities lower roughness values than the optical device. However, it is shown that by only controlling particle velocity the surface roughness can be affected.

9. Summary and outlook

It has been shown that the erosion profile of the blasted microstructure can be influenced with the nozzle configuration. The concept of a line shaped Laval nozzle, which delivers homogeneous dispersed particles with velocities in the supersonic regime, offers the best prospects for MAB processing. The validity of the presented set of models has been proven with respect to particle velocity, blasted surface profile and roughness. As a benefit of the model, the input parameters can be optimised to achieve controllable removal rate, surface quality and blasting shape.

It becomes now possible to develop a scan strategy of the nozzle to create structures with a controllable depth. The model should further be applied for different input parameters such as particle size and substrate materials.

References

[1] M. Bothen, Mikro-Abrasives-Druckluftstrahlen zum Abtragen sprödbrechender Materialien der Mikrosystemtechnik, Köster, Berlin, 2000.

[2] H. Wensink, J.W. Berenschot, H.V. Jansen, M.C. Elwenspoek, High resolution powder blast micromachining, in: Proceedings of the 13th International Workshop MEMS, Miyazaki, Japan, 2000, pp. 769–774.

[3] E. Belloy, S. Thurre, E. Walckiers, A. Sayah, M.A.M. Gijs, The introduction of powder blasting for sensor and microsystems applications, Sens. Actuators A 84 (2000) 330–337.

[4] M. Achtsnick, J. Drabbe, A.M. Hoogstrate, B. Karpuschewski, Erosion behaviour and pattern transfer accuracy of protecting masks for micro-abrasive blasting, J. Mater. Proc. Tech. 149 (1–3) (2004) 43–49.

[5] I. Finnie, Erosion of surfaces by solid particles, Wear 3 (1960) 87–103.

[6] A.N.J. Stevenson, I.M. Hutchings, The influence of nozzle length on the divergence of the erodent particle stream in a gas blast erosion rig, Wear 189 (1995) 66–69.

[7] P.H. Shipway, I.M. Hutchings, Influence of nozzle roughness on conditions in gas-blast erosion rig, Wear 162–164 (1993) 148–158.

[8] J. Wolak, P. Worm, I. Patterson, J. Bodoia, Parameters affecting the velocity of particles in an abrasive jet, J. Eng. Mater. Tech. (1977) 147–152.

[9] P.H. Shipway, I.M. Hutchings, The effect of plume divergence on the spatial distribution and magnitude of wear in gas-blast erosion, Wear 205 (1997) 169–177.

[10] M.N. Nema, P.C. Pandey, Erosion of glass when acted upon by an abrasive jet, Wear Mater. (1977) ASME 387–391.

[11] R. Balasubramaniam, J. Krishan, N. Ramakrishnan, A study on the shape of the surface generated by abrasive jet machining, J. Mater. Proc. Tech. 121 (2002) 102–106.

[12] P.J. Slikkerveer, P.C.P. Bouten, F.H. in't Veld, H. Scholten, Erosion and damage by sharp particles, Wear 217 (1998) 237–250.

[13] P.J. Slikkerveer, F.H. in't Veld, Model for patterned erosion, Wear 233–235 (1999) 377–386.

[14] M.A. Verspui, G.D. With, A. Corbijn, P.J. Slikkerveer, Simulation model for the erosion of brittle materials, Wear 233–235 (1999) 436–443.

[15] A.M. Hoogstrate, B. Karpuschewski, C.A. van Luttervelt, H.J.J. Kals, Modelling of high velocity, loose abrasive machining processes, Annals CIRP 51 (1) (2002) 263–266.

[16] G. Rudinger, Fundamentals of Gas-Particle Flow, Elsevier, Amsterdam, 1980.

[17] K. Anand, S.K. Hovis, H. Conrad, R.O. Scattergood, Flux effect in solid particle erosion, Wear 118 (1987) 243–257.

[18] B. Karpuschewski, A.M. Hoogstrate, M. Achtsnick, Simulation and improvement of the micro abrasive blasting process, Annals CIRP 53 (1) (2004) 251–254.

[19] J.D. Anderson, Fundamentals of Aerodynamics, McGraw-Hill, New York, 1991.

[20] G.S. Settles, S. Garg, A scientific view of the productivity of abrasive blasting nozzles, J. Prot. Coatings Linings (1995) 28–41.

[21] B. Bailey, J. Hiatt, Sphere drag coefficients for a broad range of Mach and Reynolds numbers, AIAA J. 10 (1972) 1436–1440.

[22] J. Nikuradse, Untersuchung über die Geschwindigkeitsverteilung in turbulenten Strömungen, Forsch.Arb. Ing.-Wes. Heft 281, Berlin, 1926.

[23] J. Westerweel, Fundamentals of digital particle image velocimetry, Meas. Sci. Technol. 8 (1997) 1379–1392.

[24] C.D. Meinhart, S.T. Wereley, J.G. Santiago, A PIV algorithm for estimating time averaged velocity fields, J. Fluids Eng. 122 (2000) 285–289.

[25] D.B. Marshall, B.R. Lawn, A.G. Evans, Elastic/Plastic indentation damage in ceramics: the lateral crack system, J. Am. Ceram. Soc. 65 (11) (1982) 561–566.

[26] R. Hill, The Mathematical Theory of Plasticity, Oxford University Press, Oxford, 1950.

[27] A.G. Evans, M.E. Gulden, M. Rosenblatt, Impact damage in brittle materials in the elastic–plastic response regime, Proc. R. Soc. A 361 (1978) 343–365.

[28] H. Wensink, M.C. Elwenspoek, A closer look at the ductile–brittle transition in solid particle erosion, Wear 253 (2002) 1035–1043.

[29] M. Papini, D. Ciampini, T. Krajac, J.K. Spelt, Computer modelling of interference effects in erosion testing: effect of plume shape, Wear 255 (2003) 85–97.